Geophysical Journal International

Geophys. J. Int. (2022) **0,** 1–16
Advance Access publication 2022 November 24
GJI Seismology

https://doi.org/10.1093/gji/ggac465

Structure of the Kathmandu basin inferred from microtremor measurements: a preliminary study

Franco Pettenati [1], Dev Khumar Maharjan,[2] Sarmila Paudyal,[2] Denis Sandron,[1] Sharad Wagle,[2] Claudio Cravos,[1] Massimo Giorgi[1] and Surya Narayan Shrestha[2]

[1] *National Institute of Oceanography and Applied Geophysics – OGS, Borgo Grotta Gigante 42/c, 34010, Sgonico, Trieste, Italy. E-mail: fpettenati@inogs.it*
[2] *National Society for Earthquake Technology - Nepal (NSET), Block P, Road CR-13, House 65, Sainbu Awas, Bhainsepati, Lalitpur Metropolitan City-25, Nepal*

Accepted 2022 November 22. Received 2022 September 26; in original form 2021 May 3

SUMMARY

This research aims at characterizing the deep sedimentary basin of Kathmandu (Nepal) from microtremor measurements, by using two surveys carried out in November 2015 and November 2018. The data collected are sufficient for a qualitative investigation of the seismic response of such a complex basin. The measurements were undertaken in the framework of a collaboration between the NSET (National Society for Earthquake Technology, Nepal) and the OGS (National Institute of Oceanography and Applied Geophysics, Italy). During the two campaigns, a series of passive seismic surveys were made, taking into consideration both single broad-band sensors and arrays. The 2015 study initially focused on the Lalitpur area (southern part of Kathmandu) and was later extended to the northern and more urbanized area of the capital city of Nepal. The 2018 survey focused on estimating the *S*-wave velocity field of the entire stratigraphic sequence by array and a repetition of some Horizontal to Vertical Spectral Ratio (HVSR) measurements close to two boreholes with reliable stratigraphy. Two inversion methods, using the data from the seismic arrays, were useful to infer the *S*-wave velocity profiles of the shallower layers and to interpret some HVSRs. The outcome is a map of the periods of single station data representing the seismic response of the basin. Comparing these results with the strong motion data of the Gorkha 2015 main shock, we confirm that the longer periods are not only the effects of the earthquake source, but also of the local response of the basin itself.

Key words: Asia; Body waves; Earthquake hazards; Seismic noise; Site effects.

1 INTRODUCTION

The seismological community turned its attention to the Kathmandu valley (Fig. 1) soon after the M_w7.8 Gorkha earthquake, which occurred on 25 April 2015. This area is densely urbanized, and the population is rapidly increasing, with a current size of around 5 million. The seismic risk in the Kathmandu valley is very high due to the occurrence of Himalayan earthquakes. The sub-horizontal discontinuity plane (Main Himalayan Thrust—MHT), generated by the underthrusting of the Indian subcontinent beneath Tibet (Molnar & Tapponnier 1975), is the major earthquake source for this area. Currently, after the Gorkha sequence, the situation has turned critical, with a locked lower edge of the MHT (Wesnousky *et al.* 2017) located just southwest of Kathmandu (Fig. 1a), putting the city in a dangerous position (Avouac *et al.* 2015; Wesnousky *et al.* 2017).

Many $M > 7$ earthquakes have struck Nepal in the historical era (Bollinger *et al.* 2014, 2016) and the aforementioned locked area is positioned between the large 1505, *M*8.5 event to the west, the 1934, *M*8.2 earthquake towards the east (Sapkota *et al.* 2013; Pettenati *et al.* 2017) and the 2015 Gorkha sequence to the north (Feng *et al.* 2015), as can be seen in Fig. 1(a). The sequence and the distribution of the associated aftershocks extended eastwards (Adhikari *et al.* 2015) from April 2015 for the following 2 yr.

The ground motion data of the Gorkha 2015 earthquake in the Kathmandu valley was recorded mainly by the HU-TU array of Hokkaido (Japan) and Tribhuvan (Kathmandu) universities. The array includes four accelerometers (Fig. 1b), installed in the southern part of the basin (Takai *et al.* 2016), and located, from east to west along the same latitude in the Kirtipur Municipality Office (KTP), the Department of Geology of Tribhuvan University (TVU), the Pulchowk Campus of Institute of Engineering (Tribhuvan University) Patan (PTN) and the University Grants Commission Office Bhaktapur (THM). Two other accelerometer stations are: KATNP (USGS permanent QNC Netquake sensor; Dixit *et al.* 2015) in the locality of Kantipath and DMG in the Department of Mines

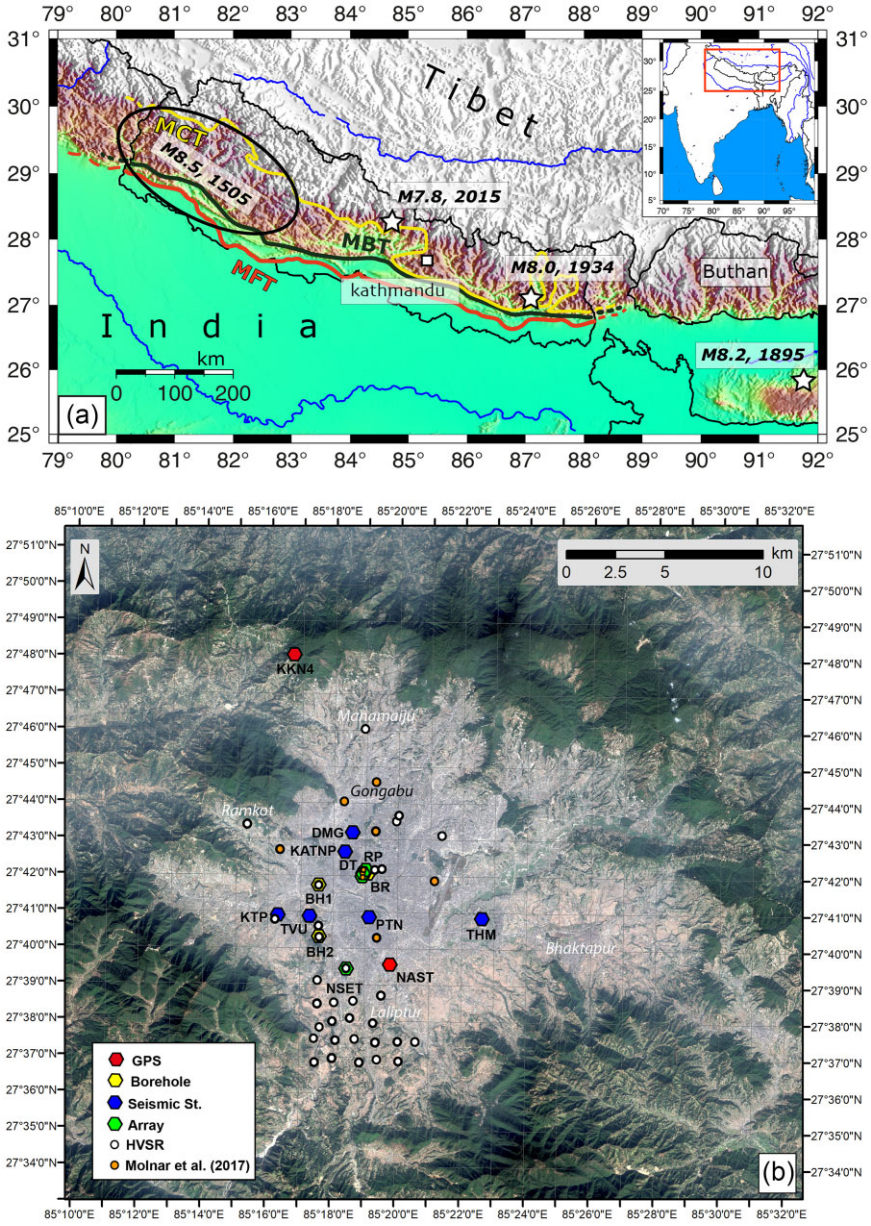

Figure 1. (a) Simplified tectonic framework of Nepal. The major structures are: the Main Central Thrust (MCT), the Main Bottom Thrust (MBT) and the Main Frontal Thrust (MFT). White stars: *M*8.2, 1895 earthquake, *M*8.0, 1934 earthquake (Sapkota *et al.* 2013; Pettenati *et al.* 2017), *M*w7.8, 2015 earthquake. The black ellipse indicates the area of the *M*8.5 event of 1505. (b) A Sentinel image (ESA Copernicus) of Kathmandu basin with the locations of the H/V measurement sites (white) and the seismological instruments installed at the time of the Gorkha earthquake: GPS stations (red), seismic stations (blue). Borehole and seismic arrays are marked in yellow and green, respectively.

& Geology (Bhattarai *et al.* 2015). Only the KTP sensor is installed on outcropping rocks on the margin outside of the basin.

The strongest Peak Ground Acceleration (PGA) recorded for the main shock was 0.255 g on the horizontal component at KTP (Bhattarai *et al.* 2015) and 0.16 g at KATNP (Dixit *et al.* 2015), while the strongest acceleration on the vertical component was 0.21 g at DMG. Ground Motion Prediction Equations (GMPE) developed for Japan underestimate observed response spectra at periods of around 4 s (Dhakal *et al.* 2016). Except for the PGA of the main shock, the PGA and Peak Ground Velocity (PGV) of the aftershocks are well described by the GMPE relations. The same result was also observed by Bhattarai *et al.* (2015).

So, for the Kathmandu basin there are two main and rather peculiar observations: the low PGA value recorded for the main shock at short distances from the rupture; and the peak spread around 4 s on the response spectra. While the first is a source effect (Rupakhety *et al.* 2017), Galetzka *et al.* (2015) were the first to hypothesize the peak energy over 3–4 s in the GPS and strong-motion data as a combination of source and site effects.

To study the seismic response of this deep basin, many investigations have been undertaken, starting with Pandey (2000) and Paudyal *et al.* (2012, 2013) with 175 Horizontal to Vertical Spectra Ratios (HVSR hereafter) performed on a 1 km grid in the most urbanized part of the city, showing a range of peak frequencies from 0.5 to 5 Hz. After the Gorkha earthquake, the investigations

proliferated: Molnar *et al.* (2017) collected several HVSRs distributed throughout the basin, some of which have the maximum peak at frequencies below 1 Hz. These authors also performed some interesting studies of surficial layer velocities by arrays. Poovarodom *et al*. (2017), by means of some arrays and using inversion methods, showed the evaluations of *S*-wave velocity (*Vs* hereafter) for each stratigraphic column. The authors compared their results with the main shock of the 2015 Gorkha strong motion data and highlighted the amplification of long periods in relation to the thickness and poorly consolidated sediments in the basin.

On November 2015, the National Institute of Oceanography and Applied Geophysics—OGS (Italy) in collaboration with the National Society for Earthquake Technology (NSET, Nepal) undertook a microtremor survey in the southern part of the Kathmandu valley (Sandron *et al.* 2019). The survey targeted the Lalitpur area that was not covered by the previous survey of Paudyal *et al.* (2012; 2013). This rural area is rapidly developing, and was severely damaged during the Gorkha earthquake. In this area, the surveys comprised HVSR and array measurements. Given the low frequencies detected in Lalitpur, much lower than those observed by Paudyal *et al.* (2012, 2013), NSET—OGS performed some other measurements in the central part of the basin, where Moribayashi & Maruo (1980) estimated a thickness of about 600 m of soft sediments. At a borehole drilled in the city centre, close to the Bhirikutimandap Exhibition Hall (BR hereafter, Fig. 1b), south of Ratna Park, the basement rock was reached at a depth of 550 m (Khadka 1993). In November 2018 the NSET—OGS focused on this well (BR), with available stratigraphy and BH1 (Sakai *et al.* 2001), located in Rabibhawan (south of Ratna Park) and with the rock basement at 252 m. Refinements of arrays were also performed to detect the near the surface *Vs* and some other HVSR sites.

All these studies do not provide a global characterization of the seismic response but at least a rough evaluation of the mean *Vs* velocity and representative stratigraphy of the basin.

The main goal of this work is to map representative periods of the seismic response of the western part of the basin (which includes the main part of the city), through our measurements and also considering the ground motion data recorded for the Gorkha event. Furthermore, this work seeks to give an interpretation of the of *Vs* structure of the basin, by comparing two methods of seismic noise inversion (Parolai *et al.* 2005 and Dinver of Wathelet 2005). With the data of 2018, Trevisani *et al.* (2020, 2021), using geostatistics analysis, with the few HVSR data available (only 39 site-points), managed to obtain information on the tectonic structure and morphology of the basement of Kathmandu basin. Similar results by borehole data, gathered in the SAFER geodatabase (Gilder *et al.* 2020), have been re-interpreted and harmonized to generate an interpolated map of the buried bedrock. Two cross sections outline the great variability of bedrock topography (fig. 7 in Gilder *et al.* 2020, SAFER hereafter). These maps depict the interesting geometry of the basement of the basin to explain its seismic response.

2 THE GEOLOGY OF THE KATHMANDU BASIN

The central Himalayan area is divided into four different geological regions by major thrusts that are assumed to be surficial expressions of the MHT that run west to east all along the Himalayan chain. The thrust farther north is the Main Central Thrust (MCT) which bounds the Higher Himalaya region in the south. The Lesser Himalaya extends from the (MCT) to the Main Boundary Thrust (MBT) in

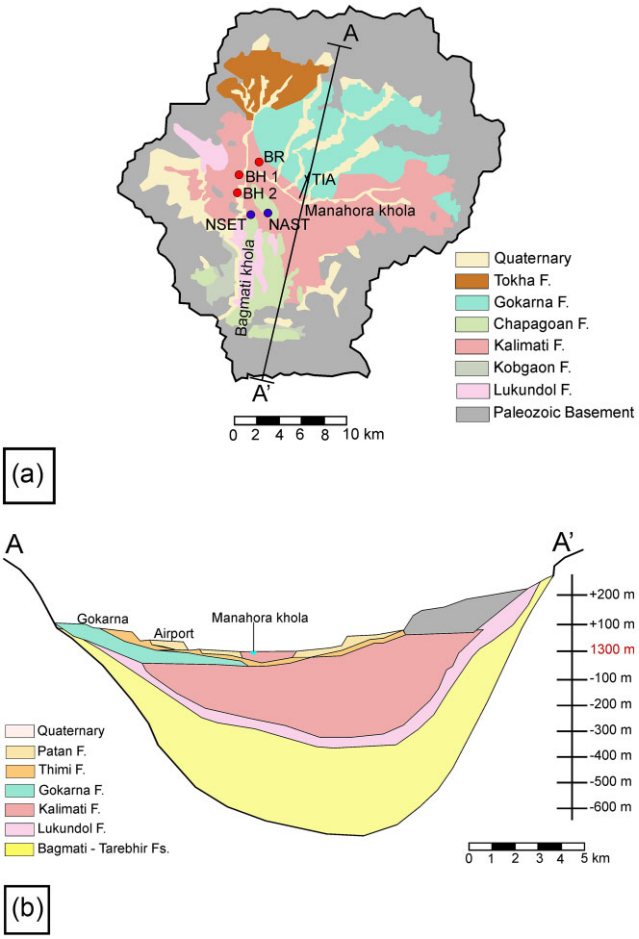

Figure 2. (a) Simplified geological map of the Kathmandu basin with the main formations, dating from the Late Pliocene to the Quaternary, surrounded by the Palaeozoic basement (Devonian). (b) East–west cross section, (through the airport zone) modified from Shrestha & Shah (2014). TIA is the Tribuvan International Airport, BR is the Bhirikutimandap Exhibition Hall. BH1 and BH2 are the boreholes used in this study along with the BR well. The black line is the approximate position of the cross section.

the south. Siwalik extends to the south until the Main Frontal Thrust (MFT), the most external expression of the MHT (Fig. 1a). To the South stretches the Indo-Gangetic plain.

The Kathmandu valley and its basin have a tectonic origin and they are included in the Lesser Himalaya. The intermountain basin of Kathmandu is filled with glacial and fluvio-lacustrine sediments. The substrate consists of meta-sedimentary bedrock of the Phulchauki Group (Paudyal *et al.* 2012—Precambrian-Palaeozoic) in the southern and central part, while gneiss, schists and granite constitute the northern slope. The sediments have a thickness of about 600 m in the middle of the basin and they date to between the Late Pliocene to the Quaternary. The depth was somewhat constrained by a gravimetric survey performed by Moribayashi & Maruo (1980). The basin formations (Sakai *et al.* 2001, 2008) from oldest to youngest are: the Dharmasthali, Kalimati, Chapagoan, Gokarna, Thimi, Tokha and Patan Groups (Figs 2a and b). Fluvial gravel and sand of the Tarebhir Fm in the south and the Bagmati Fm in the central area are the oldest and date to before 2.8 Myr (Igarashi *et al.* 1988; Sakai *et al.* 2001, 2008).

In the south, muddy sediments of the Lukundol Fm and Kobgoan Fm cover a period from 2.8 to 1 Myr, while the Chapagoan Fm dates

to the Pleistocene. In the northern part of the basin, the Gokarna Fm dates from the Middle Pleistocene. The Patan Fm is composed of fluvial deposits dating from 14 to 19 kyr (Paudyal *et al*. 2012) to 10 kyr (Last Glacial Maximum—LGM). The Gokarna Fm is made up of gravel and sands covered by silt and clays from the Thimi Fm. The most important formation is Kalimati Fm, which in Nepali means 'black mud'. This formation spans from 2.8 Myr (Late Pliocene) to 30 kyr (Pleistocene) and is the only formation distributed all over the central basin.

2.1 Glacial phase and deep correlated layer

Geological bodies often have very complex geometries, with several indentations and lateral changes (Dill *et al.* 2001). The complex geological shape of the basin is related to the seven climatic oscillations that occurred during the deposition of the older units (Igarashi *et al.* 1988). These oscillations correspond to glacial and interglacial periods, resulting in the alternation of wet and dry environments affecting the water level in the Palaeo Kathmandu Lake. During the Late Pleistocene, a glacial, cold and dry climate led to the shrinkage of the lake and controlled the deposition of sediments from the Patan Fm. Mukunda & Sakai (2008) and Mampuku *et al.* (2008) confirmed these climate changes by means of the $^{13}C/^{14}C$ ratio vegetation shifts. In simple terms, the plants fix ^{13}C through photosynthesis and during glacial phases there is an enrichment of this lighter isotope. Sakai *et al.* (2001) also reported seven cyclical oscillations from the Middle to Late Pleistocene. These authors focused their attention on a layer of sand in a rapid deposition at the end of the glacial phase, located at a depth ranging from 83 to 89 m found in the BH1 (Sakai *et al.* (2001). The stiffness of the layer increases below 83 m and further increases below 89 m. The sand layer is evidence of a high-energy depositional environment, probably related to the rapid lake emptying during the dry and cold period at the end of the glacial phase. The sedimentation rate of the formation appears to increase gradually from the lower to upper part of the sediments, except for the 83–89 m sand layer, where it is increasing with burial depth (Mampuku *et al.* 2008). The Kalimati formation is unconformably overlayed by Patan at 10.9 m in depth.

3 GROUD SHAKING DATA ON THE BASIN

Avouac *et al.* (2015) is one of the first studies on the 25 April 2015 M_w7.8 Gorkha earthquake. The authors, based on contemporary literature (Paudyal *et al.* 2012, 2013), indicated that the Resonance Period peak (RP hereafter) of the basin was believed to not exceed $T = 2$ s, concluded that the long period pulse of $T = 3$–6 s on all strong motion response spectra data was a source effect. Dixit *et al.* (2015) also noted that the PGV values were more or less consistent with the predictions, explaining the long period peaks on the KATNP acceleration response spectra as a source effect following the work of (Paudyal *et al.* 2012, 2013). Galetzka *et al.* (2015), based on the analysis of data from two GPS sites, one on the rock (KKN4, Fig. 1b) and one in the basin (NAST, Fig. 1b), along with the strong motion data of Kantipath (KATNP), were the first to hypothesize that the wide impulse is a combination of source and site effects. The authors underlined how the Gorkha earthquake induced only minor damage in vernacular dwellings, while causing severe damage or collapse in taller structures like the Dharahara tower (reaching a height of 45 m, DT in Fig. 1b). They also detected a pulse at 6–7 s in the source rupture. This peculiar pulse was also described

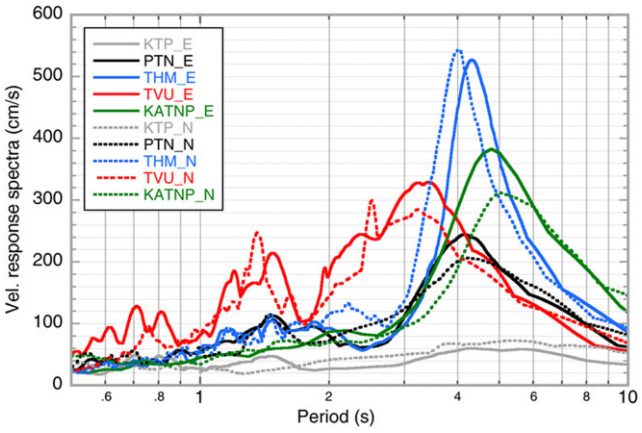

Figure 3. Horizontal components of the Gorkha earthquake *S*-waves ground velocity response spectra (5 per cent damping) recorded at the HU-TU array stations (Hokkaido—Japan) and Tribhuvan-Kathmandu Universities; Takai *et al.* 2016): KTP, PTN, THM, TVU and KATNP.

by Dhakal *et al.* (2016), Takai *et al.* (2016) and Rupakhety *et al.* (2017).

There is a dominant RP at $T \sim 4$ s on the response spectra of all the available records. The preliminary study of Bhattarai *et al.* (2015), comparing accelerations recorded at DMG and KATNP (Fig. 1b), confirms the presence of non-linear effects and low PGAs. The same authors concluded that the long periods on the response spectra are related to the rheological conditions of the basin.

According to Dhakal *et al.* (2016), quantitatively assessing the non-linearity of HVSR curves from the Degree of NonLinear response (DNL index–Noguchi & Sasatani 2008), observed that the HVSR for the main shock at $T > 0.8$ s do not show any systematic trend compared to the scattered values of the aftershocks. This suggests that the ground motion at longer periods was not affected by non-linearity. These authors then demonstrated that in the velocity seismograms of the main shock, contrary to what happens for the aftershocks of $M_w \geq 6.3$, the significant ground motion does not continue for an extended duration because the direct arrivals had very large amplitudes at periods slightly larger than the site resonance period around 4 s, due to of the strong pulse-like input ground motions with periods of 6–7 s at the base of the sediments. Dhakal *et al.* (2016) then proposed a 1-D velocity model to explain the long period pulse with a peak at $T = 4$ s.

Takai *et al.* (2016), analysing the four HU-TU accelerometers (Fig. 1b) considered the single pulse in the ground velocity of the rock site KTP (integrated to displacement) as a monotonic step associated with the permanent tectonic offset. Moreover, they detect that the displacement waveforms of KTP were like those of KKN4 GPS on the rock site, which is located further north and closer to the epicentral zone. The same impulse is present on the vertical velocity records of the three stations HU-TU on sediments and on the KATNP record. In contrast, at three sedimentary sites, both the horizontal ground velocities and accelerations observed showed long duration with conspicuous long-period oscillations, due to the valley response. The horizontal valley response was characterized by large amplifications and prolonged oscillations which differ from site to site showing the complex structure of the basin. The horizontal component of ground velocities of these four stations shows long RP ($T = 3$–6 s) in Fig. 3 and are seen to be spread in the THM, KATNP and TVU records, but are less prominent and low in the PTN records, confirming the behaviour of the basin. Regarding the vertical component of ground velocities at the sedimentary

sites, Takai *et al.* (2016) indicate that they were nearly the same as those observed at KTP station. Rupakhety *et al.* (2017), emphasizing the presence of long-period resonance peaks on the HU-TU and KATNP records, also suggested a period peak around T = 4 s (Fig. 3). Interesting are the 5 per cent damped acceleration response spectra which are rotation-invariant with respect to horizontal directions. This rotation-invariance is overall visible on the long periods where there is a peak around 5 s. These authors analysed the polarisation of the long period pulse of the KATNP record (basin) and of KTP (basement). For KATNP, the pulse is not a Rayleigh wave; the polarisation pattern at KATNP is more like that of Love waves.

4 METHODS, INSTRUMENTS AND SURVEYS

4.1 Microtremor methodologies

The resonance frequencies of the basin were studied using the well-known HVSR method (Nakamura 1989, 2019) which is based on the calculation of the ratio between the horizontal and vertical Fourier amplitude spectra of microtremors recorded using a single station. It is often referred to as the 'Nakamura' method, even though it was initially introduced by Nogoshi & Igarashi (1971) along with the first explanation of the nature of environmental noise and the origin of microtremors. A recent review on this is provided by Bonnefoy-Claudet *et al.* (2006a). The body waves, in the case of an impedance contrast, are predominant below the resonance frequency (f_0) of the SH waves, while the Rayleigh waves increase from f_0 to $2f_0$, reaching a maximum (Nakamura 2000; Bonnefoy-Claudet *et al.* 2006b). Significant peaks are often present in the microtremor spectra, around f_0 in all the spatial components (Z, E, N). This is a result of multi-reflection of SH waves trapped within soft-layered media overlying a rigid bedrock. Konno & Omachi (1998) showed that there are three types of HVSR of the fundamental mode of Rayleigh waves, with one peak and zero, one or two troughs. They found that the HVSR tends to show the peak/trough structure when the surface soils are soft. They investigated the relationship between the periods of peaks (*Tp*) and troughs (*Tt*) and found that the *Tp* of the fundamental mode Rayleigh waves match the fundamental period of the transfer function for vertically incident *Vs*, in the case of a strong impedance contrast. Recent studies (e.g. Tuan *et al.* 2011) concluded that the peak/trough structure is the response of near surface deposits with a high-Poisson ratio associated with an underlying bedrock interface, leading to a high impedance contrast.

Knowledge of the SH-wave velocity, combined with HVSR resonance frequency values, is fundamental to infer the thickness of a geological structure. Some geophysical methods use both active and passive seismic techniques to exploit the dispersion, a well-known property of surface waves. Dispersion in a wave train (Bäth 1973) occurs when different frequencies travel at different velocities (called 'phase velocity'). According to Park *et al.* (1997), phase velocity depends primarily on the shear wave velocity of the medium and it is slightly influenced by compressional wave velocity, density and Poisson's ratio. Therefore, the surface wave velocity is a good indicator of *Vs*. Normally, the phase velocity of surface waves is in the range between 88 and 95 per cent of *Vs* for any value of Poisson's ratio (Ewing *et al*. 1957). The main passive methods used to study the dispersion curves are SPAC (Spatial Auto Correlation method, Aki 1957) and its extension MSPAC (Bettig *et al.* 2001). Other methods are based on the frequency–wavenumber (*f*–*k*) spectral analysis (Capon 1969) or ReMi^{TM} (Refraction Microtremors, Louie 2001) technique.

The MSPAC method estimates the Rayleigh Phase Velocities (V_{RP}) by fitting, for each frequency, the spatial-correlation function to a Bessel function, which in turn depends on the interstation distances. This is because the waves are statistically independent (Boxberger *et al.* 2011) and the V_{RP} are a function of frequency. Using the Wiener–Khinchin theorem, which establishes that the same information on the phase shift can be obtained using the spectra of the signal measured at two sensors, enables development of the coherence function. The set of these function values is named 'coherence matrix' for the different pairs of sensors and returns information on the phase differences.

ReMi^{TM} is a technique used to assess shallow shear wave velocities by a simple 2-D slowness-frequency transform of microtremor records to separate the Rayleigh waves from other seismic arrivals, using common seismic refraction recording equipment. The basic transform used in this velocity spectral analysis is the 'slant stack' in the '*Tau-P*' domain.

Regarding the inversion problems, Arai & Tokimatsu (2004) demonstrated that it is possible to retrieve the layer thickness of *Vs* profiles from inversions of HVSR curve and showed (Arai & Tokimatsu 2005) the benefits of joint inversion. Hobiger *et al.* (2013) address the problem of non-uniqueness result in the inversion of Rayleigh wave dispersion curves by integrating *Vs* information from other kinds of geophysical measurements, such as SPAC.

4.2 Instrumentation and software

In the 2015 survey (Sandron *et al.* 2019), single station data were collected with Nanometrics and MoHo equipment. The Nanometrics system is comprised of a Centaur console with a Trillium 20 s seismometer, while the MoHo system integrates a console and a 4.5 Hz Tromino® sensor. The sampling rate was fixed at 100 Hz for the two systems. The ultraportable digital seismic acquisition system SoilSpy Rosina was used as seismic ReMi^{TM} arrays to collect multichannel data. Ten geophones were placed at 5 m spacing.

In the 2018 survey, the single station equipment was comprised of two Lennartz 3DLite 1 s, while Cube-3ch-recorders, manufactured by Omnirecs (GIPP group GFZ Potsdam) and equipped with a set of PE-6/B-3C-4.5 Hz and Vertical 4.5 Hz geophones, were used as the seismic array.

Similarly to Sandron *et al.* (2019), data were processed in agreement with SESAME (2004) guidelines via the open source Geopsy package (www.geopsy.org, last accessed December 2021).

The dispersion curves of 2015 (Sandron *et al.* 2019) were processed by the ReMi^{TM} method of Grilla software developed by MoHo. We followed the scheme of SESAME (2004) to show the uncertainties of HVSR curves, computing the standard deviation for each frequency from the time series of measurements.

To solve the inverse problem, we applied two different software packages: Dinver, included in the Geopsy package (Wathelet 2005), used for the dispersion curves; and the code developed by Parolai *et al.* (2005), used both for the dispersion curves and HVSR. Both software packages use a modified Monte Carlo technique to perform the inversion. The former performs the inversion by the Neighbourhood Algorithm of Sambridge (1999), while the latter, using the Genetic Algorithms, allows the inversion of the HVSR, or in combination with the Rayleigh or Love wave dispersion curves. For uncertainties of the inversions, we used the relative patterns of the two methods used: the representation of Wathelet (2005) and the

Table 1. HVSR main resonant period *T* (s) and frequency (Hz) values from the NSET-OGS 2015 and 2018 surveys, plus some measurements from Molnar *et al.* (2017) and Paudyal *et al.* (2013). This last site was chosen as it was close to the structure towards the west. The first column is the numeration of sites, referenced to Fig. 4.

No	Longitude E	Latitude N	Frequency [Hz]	Period [s]	Instrument	Site
1	85.2921	27.6432	0.49 ± 0.09	2.040	2015	S1/S
2	85.3010	27.6437	0.28 ± 0.09	3.570	2015	S2/S
3	85.3113	27.6445	0.37	2.700	2015	S3/S
4	85.3262	27.6469	0.26 ± 0.02	3.840	2015	S4/S
5	85.2934	27.6325	0.48 ± 0.06	2.080	2015	S5/S
6	85.3003	27.6353	0.38 ± 0.09	2.630	2015	S6/S
7	85.3096	27.6367	0.41 ± 0.07	2.440	2015	S7/S
8	85.3219	27.6346	0.31 ± 0.05	3.220	2015	S8/S
9	85.2907	27.6275	0.42 ± 0.06	2.380	2015	S9/S
10	85.3020	27.6268	0.41 ± 0.08	2.440	2015	S10/S
11	85.3121	27.6274	0.35 ± 0.07	2.860	2015	S11/S
12	85.3233	27.6258	0.31 ± 0.05	3.230	2015	S12/S
13	85.3348	27.6261	0.50 ± 0.09	2.000	2015	S13/S
14	85.3442	27.6261	0.28 ± 0.06	3.570	2015	S14/S
15	85.2911	27.6167	5.30± 3.27	0.189	2015	S15/S
16	85.3002	27.6187	0.63 ± 0.08	1.590	2015	S16/S
17	85.3148	27.6167	0.42 ± 0.09	2.380	2015	S17/S
18	85.3240	27.6181	0.53 ± 0.02	1.880	2015	S18/S
19	85.3355	27.6173	0.30 ± 0.06	3.330	2015	S19/S
20	85.2924	27.6538	10.0 ± 2.5	0.100	2018	P13-03 #
21	85.3075	27.6580	0.29 ± 0.05	3.450	2015–2018	NSET*
22	85.2932	27.6726	0.30 ± 0.05	3.450	2015	BH2/S
23	85.3237	27.6730	0.39	2.560	Tromino® 3G	Patan/M
24	85.2928	27.6781	0.30 ± 0.06	3.330	2018	Tribuvan U*
25	85.2928	27.6960	0.60 ± 0.10	1.656	2018	BH1*
26	85.3223	27.7037	0.30	3.333	Tromino® 3G	Coin M.F./M
27	85.3158	27.7000	0.30	3.332	Tromino® 3G	Dharahara T/M
28	85.3160	27.7038	0.28	3.571	Tromino® 3G	Durbar S./M
29	85.3163	27.7035	0.31	3.220	Tromino® 3G	Durbar S.R./M
30	85.3160	27.7020	0.27 ± 0.04	3.700	2015–2018	Ratna Park*/S
31	85.3260	27.7040	0.22 ± 0.06	4.540	2015	DilliBazar*/S
32	85.3539	27.6985	0.85	1.170	Tromino® 3G	Airport/M
33	85.2760	27.7126	0.90	1.110	Tromino® 3G	Sita Paila/M
34	85.2930	27.7141	3.00± 0.78	0.333	Tromino® 2015	Base Swayambo untah hill
35	85.3226	27.7208	0.34	2.942	Tromino® 3G	Lazimpat/M
36	85.3579	27.7191	0.649± 0.170	1.540	Tromino® 2015	Bhoudanath/S
37	85.2545	27.7240	1.89 ± 0.19	0.530	Tromino® 2015	Ramkot/S
38	85.3339	27.7255	0.34 ± 0.05	2.940	2018	Baluwatal
39	85.3350	27.7280	0.32 ± 0.04	3.120	2018	Apeiron HQ*
40	85.3080	27.7360	0.92	1.087	Tromino® 3G	Balajou/M
41	85.3230	27.7395	0.74	1.351	Tromino® 3G	Dhapasi/M
42	85.3167	27.7667	0.813± 0.080	1.230	Tromino® 2015	Manamaiju/S

2015 = Trillium 20 s–2018 = Lennartz 1 s or PE-6/B-3C-4.5 Hz–2015–2018 = Trillium 20 s or Lennartz 1 s.
*This study -/M Molnar *et al.* (2017) [they do not provide to the errors]—# Paudyal *et al.* (2013) and this study -/S Sandron *et al.* (2019).

one proposed by Parolai *et al.* (2019), also providing the error on the peak frequencies, derived from the standard deviation of the solutions generated by Genetic Algorithm and selected based on fitness (90 per cent of total solution starting from best-fitting solution).

4.3 The data set

Our dataset covers the western part of the Kathmandu basin from north (Manamaju) to south (Laliptur; Fig. 1b). We considered a total of 42 HVSR sites (small circles in Fig. 1b): 27 sites were part of the 2015 NSET-OGS campaign, 5 more points were collected in the 2018 and 10 additional sites are from Molnar *et al.* (2017). We selected the sites with the highest quality data (Table 1): with a clear resonance peak (with amplitude greater than 2 in accordance with the SESAME (2004) guidelines) and from seismic noise recording traces lasting 60 min on average (in a range of 40 to 1 hr 30 min). In detail, from Molnar *et al.* (2017, fig. 3b), we used recordings from two HVSR stations along a slope in Sita Paila (the lowest ones to avoid the topographic effects); HVSR of the Sewage Plant array was discarded (Molnar *et al.* 2017, fig. 3a) because it has a large flat plateau in the range 1.2–1.6 Hz. We also discarded the site Balkhu because it is close to the BH1 borehole and Gongabu, (Molnar *et al.* 2017, fig. 3b) because it is close to Balajou that has a more noticeable peak.

In 2018, we repeated the HVSR measurement on site 03 of Paudyal *et al.* (2013), near the western boarder of the basin. Three HVSRs were collected near the boreholes for which stratigraphy or logging data are available (Fig. 1b): the first is BH1 (Paudyal

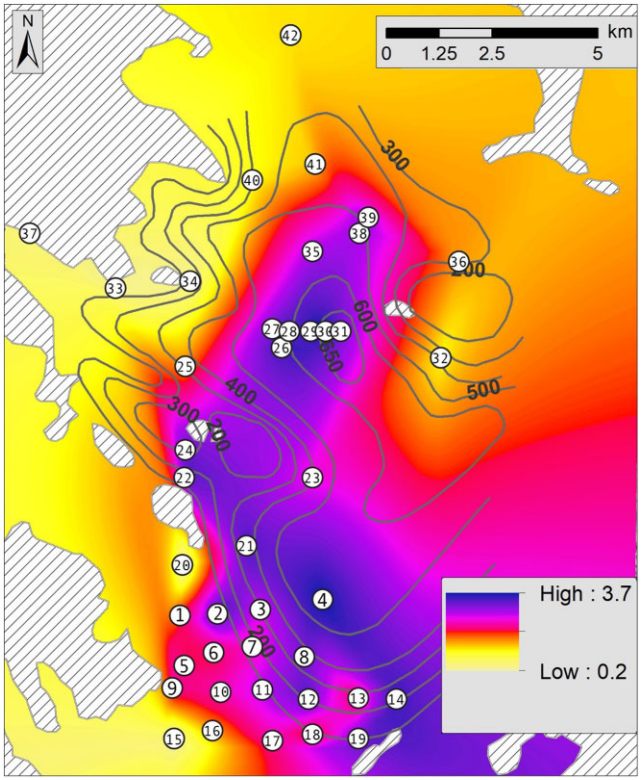

Figure 4. Map of the resonant periods RP interpolated by the Natural Neighbour method (NN, Sibson 1980). The isopach contours are based on the gravimetric survey of Moribayashi & Maruo (1980). The sites have the same number as shown in Table 1.

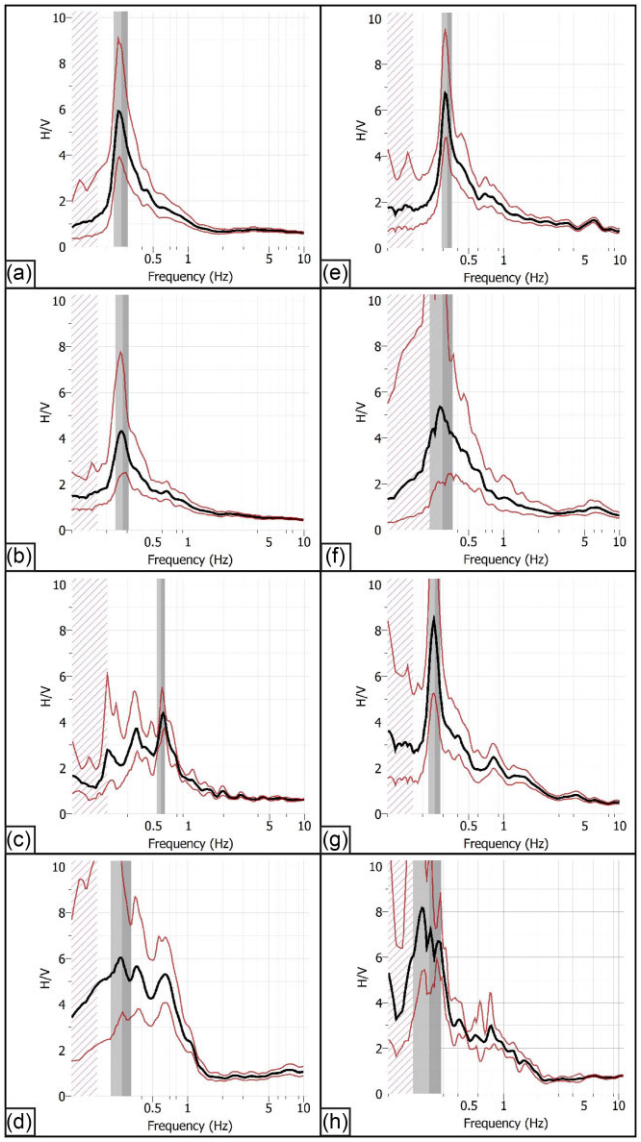

Figure 5. Examples of HVSR at: (a) Ratna Park (with PE-6/B-3C-4.5 Hz); (b) Ratna Park (with Lennartz 1 s); (c) BH1 (with Lennartz 1 s); (d) BH2 (with Trillium 20 s); (e) Apeiron House (with Lennartz 1 s); (f) NSET (with PE-6/B-3C-4.5 Hz); (g) S04 (with Trillium 20 s) and (h) TVU, Tribuvan University Campus (with Lennartz 1 s). The shaded areas mark the frequency peak and uncertainty, reported in Table 1; the cross hatching on the left indicates the band of least reliability of the data.

et al. 2012), the second is at Bhrikutimandap Exhibition Hall (BR in Fig. 1b), near Ratna Park (RP in Fig. 1b), which reaches the basement, and the third is close to the NSET headquarters (NSET HQ hereafter). An additional HVSR station was recorded in 2015 close to borehole BH2, with the stratigraphy of BH1 and BH2 reported in Paudyal *et al.* (2013). Khadka (1993) report on the Bhrikutimandap well, while the logging stratigraphy of the borehole at the NSET HQ is provided by Sandron *et al.* (2019, table 2).

The RPs of the resonance peaks, sorted by the equipment used are summarized in the Supporting Information (Fig. S1a): the histogram shows the predominance of periods RP around 2–4 (s). Parolai *et al.* (2001) describe a term of comparison between H/V curves recorded by different sensors.

The passive seismic arrays data collected in 2018 are located at Ratna Park (RP in Fig. 1b), at the park of Tribhuvan University (TVU in Fig. 1b), and close to the NSET HQ. We adopted a 'star' configuration for the seven sensors used. In Ratna Park, one of the sensors failed and therefore the configuration shown in Fig. S1(b) was used, with a maximum aperture of 80 m. In the site close to the NSET HQ, we used the array from the 2015 campaign (Sandron *et al.* 2019) with an 'L' shape configuration.

5 RESULTS

The sparse RPs measured in the valley were interpolated using the Natural Neighbour method (hereafter NN, Sibson 1981) to generate a map (Fig. 4).

The site of Ramkot (n. 37 in Fig. 4 and Table 1) is in the shallower part of the basin where liquefaction occurred during the 2015 earthquake (see Section 3.1). In Boudhanath (n. 36), north of the airport area, the HVSR curves are similar to those from Molnar *et al.* (2017, fig. 3a). Table 1 reports the position, frequencies (*f*), periods (T) and instrumentation used for each site. Fig. 4 also shows the contour levels of the bedrock depth by the gravimetric survey of Moribayashi & Maruo (1980). The two basement maxima with depths greater than 500 m of the Moribayashi & Maruo (1980) map are consistent with the two maxima of the RP (interpreted to be a proxy of the basement depth).

In Fig. 5, we also document some other significant HVSR curves, as the comparison of the data collected in Ratna Park (n. 30 in Fig. 4) with different sensors (Figs 5a and b) is particularly relevant notwithstanding the different response of the sensors. All peaks in the very low frequency interval are sharp with high kurtosis, which show the consistency and reproducibility of the data. The

Table 2. Bedrock depths resulting from the HVSR inversion of selected sites. H = bedrock depth (m); Vs = S-wave velocity (m s^{-1}); ρ = density (kg m^{-3}); σ = ranges of Poisson's ratio used for inversion. The ranges of depths are narrow (±10 m). For each site: row 1 calculation by simple formula; rows 2–3 inversion (Parolai *et al.* 2005) by tight constraints; rows 4–5 inversion (Parolai *et al.* 2005) by fixed basin thickness.

Site/calculation	Layer	H [m]	Vs [m s^{-1}]	ρ [kg m^{-3}]	σ	Thick range	Vs range	Fitness
BH1								
by $Vs = 4\,H\,f$	basin	252*	605					
tight constr.	basin	255	610 ± 9	1.9	0.45	250–300	500–700	0.24335
inversion	bedrock		853 ± 29	2.4	0.41		600–2000	
fixed thick	basin	252*	604	1.9	0.45			0.24344
inversion	bedrock		845	2.4	0.41			
Ratna Park								
by $Vs = 4\,H\,f$	basin	549**	605					
tight constr.	basin	543	647 ± 8	1.9	0.46	1–800	300–1000	0.30758
inversion	bedrock		936 ± 21	2.5	0.39		600–2000	
fixed thick	basin	549**	672	1.9	0.46			0.31490
inversion	bedrock		944	2.5	0.39			

Depth from: *Sakai *et al.* (2001); **Khadka (1993).

stability and the consistency of the measurements can also be verified with the 2015 survey results outlined in Sandron *et al.* (2019). Moreover, in Figs 5(c)–(h) can be seen: the measurements close to the boreholes BH1 Fig. 5(c), BH2 Fig. 5(d); another very low frequency peak (Apeiron House, Fig. 5e); the NSET HQ Fig. 5(f), S04 (Fig. 5g) and Tribuvan University campus (Fig. 5h). This last HVSR is comparable with the PGV response spectra in Fig. 3. Unfortunately, the distribution of the sites is not uniform, with a cluster in the south and scattered points in the north.

Taking advantage of the HVSR measurements carried out near the two wells that reach the basement in BH1 (see in Fig. S2(a) one peak HVSR achieved by PE-6/B-3C-4.5 Hz) and Ratna Park (Fig. 5b), nearby BR (Khadka 1993), we can apply the general formula $Vs = 4\,H\,f$ to estimate the average shear wave velocity of the entire stratigraphic sequence. The relative depth–frequency values are $H = 252$ m and $f = 0.60$ Hz for BH1 and $H = 549$ m and $f = 0.275$ Hz for BR (see Table 1). The resulting velocities are therefore both $Vs = 605$ m s^{-1}. To confirm this value, we used the method suggested by Parolai *et al.* (2005) to invert the Rayleigh ellipticity curves and present the results in Table 2 and Figs S2(a) and S2(b) (see also Section 6). Although the simulated peaks are smaller than experimental ones, their widths are similar.

We also analysed the azimuth dependence of the HVSRs in Figs 6: Ratna Park 6(a), Apeiron 6(b), Baluwatal 6(c), BH1 6(d), BH2 6(e) and Manamajiu 6(f). The analysis for the Ratna Park site is striking and shows the azimuth independence like the other sites for which a great thickness is expected (Figs 6b and c). Other considerations are referred to Section 6.

To assess the Vs in the shallower layers, we first inverted the ReMi^{TM} dispersion curve (Fig. 7) close to the wells of the NSET HQ (n. 21 Fig. 4) and the MSPAC of Ratna Park (n. 30 Fig. 4 see also Fig. S1b). From the former well, the logging stratigraphy of the uppermost 30 m is visible in Table 3 (subplot columns 1–4 from the left). We simplified the eight-layer model into a four-layer model by grouping neighbouring and similar layers two by two, whose velocity are the average weighted with thickness (columns 5–7 of Table 3). The geophone spacing in the ReMi^{TM} configuration was 5 m, so the maximum resolution is around 5 m (Foti *et al.* 2018). The last layer ($Vs = 313$ m s^{-1}) is not limited at the bottom and was not included in the modelling. Moreover, the ReMi^{TM} array has an L-shape with 25 m maximum length, thus reducing the maximum wavelength that could be identified. Based on these considerations, we carefully assume that the maximum depth of investigation is not over 50 m. We only use tight constraints only for first layer Vs (130–150 m s^{-1}); using the dispersion curves and the HVSR, the simplified model has been inverted using the Parolai *et al.* (2005) method (Fig. 7a) and by the Dinver module of the Geopsy package (Fig. 7b). The results are reported in Table 3 (last right-hand columns) and summarized in Fig. 7(c). We also inverted the dispersion curve (Fig. 7d and e) of the Ratna Park array, always with the same constraints for the first layer. The outcome is summarized in Table 4 and the velocity profiles in Fig. 7(f).

Following the same outline, we also used ReMi^{TM} data collected during the 2015 campaign (Sandron *et al.* 2019) to better constrain Vs in the shallower layers. ReMi^{TM} Vs profiles for five selected sites (S15, S17, S12, S04, BH2), are presented in Figs 8(a)–(e) (site code numbers in Fig. 4 are reported in Table 1). Only for S15 and S17 were we able to invert the HVSR jointly with the dispersion curves (Figs S3), because for the high frequencies we have peaks with amplitude over 2 and for BH2 we report here the joint inversion by Grilla performed in Sandron *et al.* (2019). The remaining inversions were carried out using the method of Parolai *et al.* (2005) and the comparison between the calculated and experimental Rayleigh dispersion curves are provided in Figs 8(f)–(j). The resulting vertical Vs profiles are presented in Figs 8(k)–(o). By these inversions, an uppermost low velocity layer stands out with Vs between 120 and 160 m s^{-1}, lying over a second layer with Vs of about 200–400 m s^{-1}. The topsoil layer in S12 site is missing, and it confirms the Vs of the second layer and shows a Vs around 400 m s^{-1} for the layer below. These data are comparable with the inversion carried out on the data of the NSET HQ and Ratna Park. The data are summarized in Table S1.

In the light of paragraph 2.1, the multiple and high-amplitude >1 RPs in the HVSR curves could be used to interpret the changes of impedance within the sediments inside the basin. The main evidence is the important peak for the borehole BH2, at frequency $f = 0.68$ Hz (Figs 5d and 9d) which cannot be connected to basement, as already explained in by Sandron *et al.* (2019). Considering the Vs = 605–650 m s^{-1} of Table 2, the basement depth would be 222–239 m, but the BH2 well reaches 280 m without intercepting it. The site S16 has a second peak at $f = 1$ Hz (Fig. 9a), while S02 has an important second peak at $f = 1.2$ Hz and a third at $f = 2.7$ Hz (Fig. 9b). We also consider the weak peaks of NSET HVSR (Fig. 9c). In Fig. 9(e) (see also Fig. 5b) the Ratna Park HVSR, is considered as the case in the deepest part of the Basin with a second frequency peak of $f = 0.68$ Hz. The inversions consider the assessment of the previous inversions of the basement Vs and the average velocity of the basin sediments, but we avoid using tight constraints. For

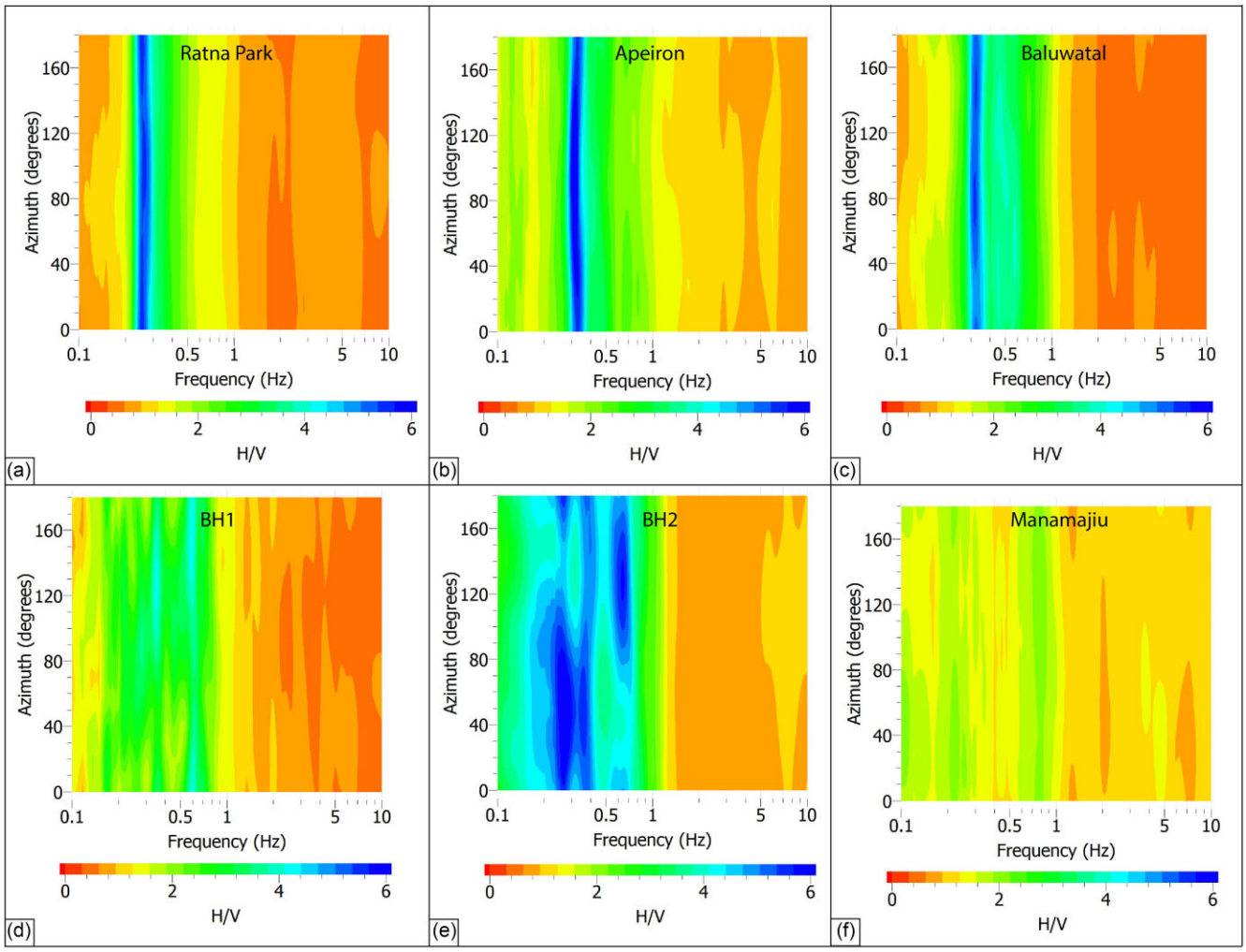

Figure 6. HVSR azimuthal spectra in: (a) Ratna Park; (b) Apeiron house; (c) Baluwatal; (d) BH1 well; (e) BH2 well; (f) Manamajiu. (a), (b) and (c) with peaks over value 5 (see Fig. 5) show the independence from the azimuth. In BH1 (d) the peaks are around value 4 and are the two cyan spots at $f = 0.6$ and 0.35 Hz (Fig. 5c). The prominent peak of BH2 at 0.68 Hz (Fig. 5d) is dependent to azimuth, the same the main peak at 0.3 Hz. Manamajiu with its peak over 1 Hz is independent on the azimuth.

site S16 the inversion is limited to the first part of the stratigraphic sequence, while BH2 takes into account the outcome of Figs 8(a), (f) and (k). The depths versus *Vs* profiles of inversions are reported in Figs 9(f)–(j). The jump of *Vs* from lower values of 400–600 m s^{-1} at depth more than 80 m can clearly be seen. Table S2 reports all the inversions also for sites S10. S6, Tribuvan campus (TVU) and BH1. Fig. S4 reports a possible trend of this hypothetic stratigraphic boundary (dotted lines) for all these sites in line from south to north in the West part of the basin (see Fig. 4).

Fig. 10 resumes all the sites where we have the spectral azimuthal plot, compared with the deepest area of the basin which we detected. The contour curve delimits the RP of 2 s which corresponds to depth more than 300 m.

6 DISCUSSION

In the strong-motion data of the 25 April 2015 Gorkha earthquake the presence of a pulse of periods between 3 and 6 s is clearly established. Galetzka *et al.* (2015) were the first to hypothesize these peaks as a combination of the earthquake's source and basin response effect. In fact, Bhattarai *et al.* (2015) and Dhakal *et al.* (2016) show that this kind of pulse is also evident in the response spectra of some major aftershocks, a sign that it cannot just be a source effect. The other important question raised from strong motion data (Takai *et al.* 2016) is that the predominant period and envelope shape of the horizontal oscillation differed not only from site to site, but also between NS and EW components. These features show that the long period response of the Kathmandu valley is complex.

The first purpose of the 2015 campaign (NSET–OGS) was to fill the gap of HVSR coverage in the Lalitpur area (Paudyal *et al.* 2012, 2013). Our study, in the light of the longer RPs reported in the Lalitpur area with respect to previous studies, also focused on the central part of the basin where the long-period RPs in the HVSR spectra suggest a larger basement depth (Table 1, Fig. 5). This result was confirmed by the integrative measures conducted in 2018. The NN map in Fig. 4 confirms the distribution of RP of values over $T =$ 2 s, with two zones having maxima over $T = 3$ s, but also areas with great variability as highlighted in the basin sections of the SAFER model (Gilder *et al.* 2020, their fig. 7), and in Moribayashi & Maruo (1980). Our map in Fig. 4, as already shown in Trevisani *et al.* (2020) by Kriging, intended as a proxy of the basement depth [following the example of SAFER maps, fig. 6(e) and sections in fig. 7(c) in

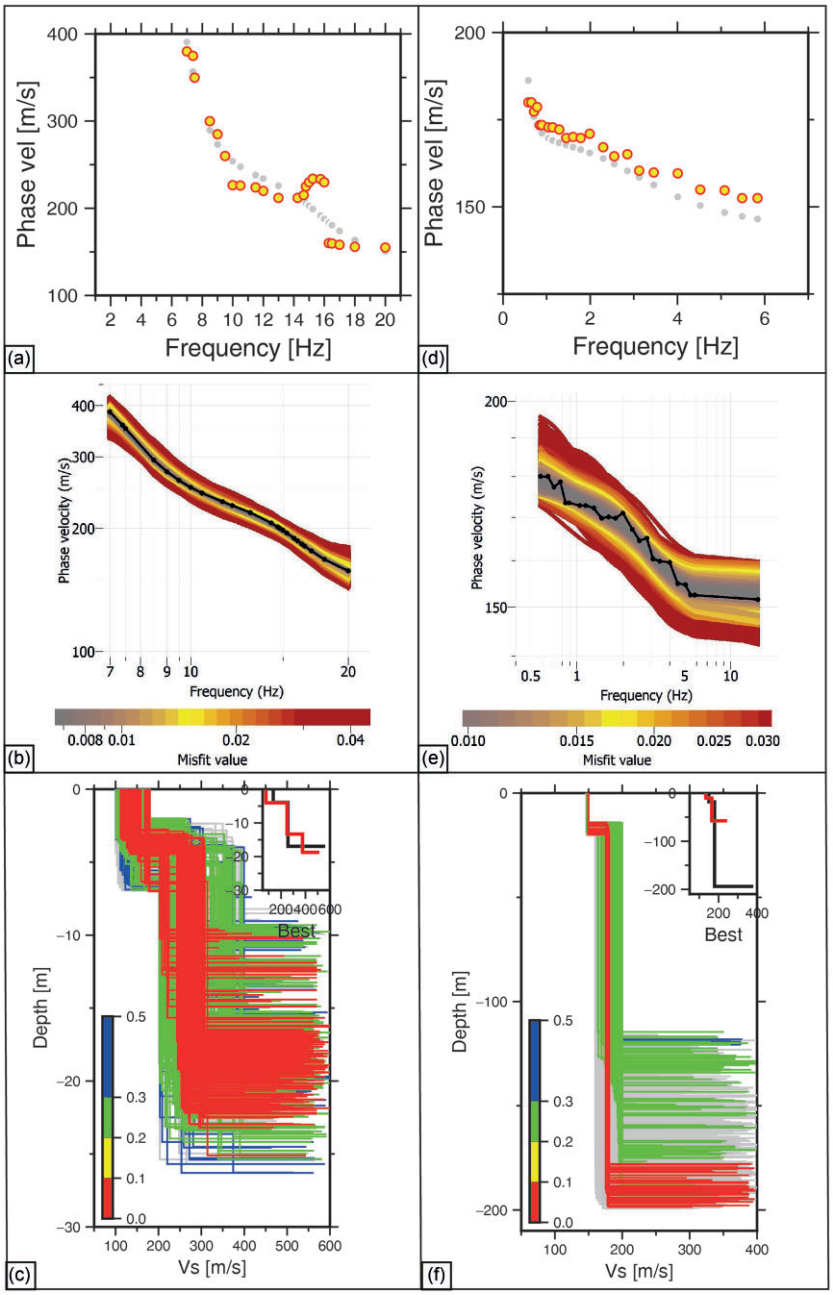

Figure 7. (a) ReMi^{TM} dispersion curve collected in 2015 at the NSET headquarter (yellow dots) and forward model by the software Parolai *et al.* 2005 (grey dots); (b) phase velocity results by Dinver of Geopsy; (c) resulting *Vs* profile of inversion (colours indicate models lying within a certain percentage of the minimum misfit). In the small box: black profile represents the minimum misfit model by the software Parolai *et al.* 2005; while red profile is the minimum misfit model by Dinver of Geopsy. (d) ReMi^{TM} of Ratna Park array 2018 (yellow dots) and forward model by the software Parolai *et al.* 2005 (grey dots); (e) phase velocity results by Dinver; (f) resulting *Vs* profiles: Parolai *et al.* 2005 with the same mode of representation as in Fig. 7(c).

their paper], shows the variability of the basement topography and the zone of maximum (depth). There are some differences among the three contour maps, but we recall that the Natural Neighbour (NN) interpolation does not introduce subjectivity because it is parameter-free, while the Kriging map, used also in SAFER, is the result of data processing (for Moribayashi & Maruo 1980, the interpolation method is unknown). In any case, the two local maxima in Moribayashi & Maruo (1980) are also reproduced by the NN map that shows one maximum in the centre of the basin and a second elongated SE–NW maximum, with a top on the S04 site (Fig. 5g). Moreover, the NN map of Fig. 4 shows a variability of RP values in the Lalitpur area (southern part), where the SAFER and Moribayashi & Maruo (1980) maps are smooth because they do not have data. This variability of the RPs in the Lalitpur area (Fig. 4), and possibly in some parts of the basin, is visible with distance, even for those less than the maximum resonance wavelength: $\lambda_{mr} = (605, 650)/0.27 \sim$ (2200, 2400 m).

The Lalitpur area is within a zone of fluvial erosion in the Pliocene formations (Shrestha & Shah 2014). Our NN map is also in agreement with a previous geostatistics interpretation of the basement topography reported in Trevisani *et al.* (2021), where the two zones of maximum RP values, are separated by abrupt variations of the

Table 3. Inversion results for the NSET headquarters. Borehole logs and simplified model (first two columns). Model obtained via Parolai *et al.* (2005) inversion method (third column). Model obtained using the Dinver inversion method (right-hand column). The results on the right-hand columns. In the last row, '?' means that the inversion results are only indicative for the large constraints of the inversion. The depths are reported in the brackets ().

							Model Parolai *et al.* 2005 results Fitness = 0.0944		Model Dinver® Fitness = 0.0048	
	Borehole logging			Simplified model						
TH [m]	*Vs* [m s^{-1}]	ρ [kg m^{-3}]	σ	*Vs* [m s^{-1}]	ρ [kg m^{-3}]	σ	TH [m]	*Vs* [m s^{-1}]	TH [m]	*Vs* [m s^{-1}]
2	100	1.5	0.450	143	1.5	0.48	4	136 ± 1	4	125
6 (8)	157	1.5	0.487							
6 (14)	333	1.7–1.9	0.437–0.474	300	1.8	0.46	13 ± 3 (17)	257 ± 13	10.5 (14.5)	245
2 (16)	200	1.9	0.490							
6 (22)	363	2.0	0.468	394	2.0	0.45			4(18.5)	372
2 (24)	486	2.0	0.440							
6-?	313	1.7	0.500	300	2.1	0.44		561 ± 56		495?

TH = thickness (m); *Vs* = *S*-wave velocity (m s^{-1}); ρ = density (kg m^{-3}); σ = Poisson's ratio.

Table 4. Near surface stratigraphy from Khadka 1993 at Ratna Park (left column). the inversion results for Ratna Park used the Parolai *et al.* (2005) and Dinver® approaches. The depths are reported in the brackets (). '?' means that the inversion results are only indicative for the large constraints of the inversion.

		Model Parolai *et al.* 2005 Fitness = 0.0 1287		Model Dinver® Fitness = 0.0 1424		ρ and σ for both models	
Model from Khadka (1993)							
TH [m]	Type	TH [m]	*Vs* [m s^{-1}]	TH [m]	*Vs* [m s^{-1}]	ρ [kg m^{-3}]	σ
20	Coarse grained sand	18 ± 2	150 ± 1	15	125–130	1.5	0.48
153 (173)	Greenish grey clays	176 ± 20 (194)	180 ± 8	50 (65)	165	1.9	0.46
6 (179)	**						
28	Greenish grey clays						
?			380 ± 49		224	2.0	0.43

TH = thickness range (m); *Vs* = *S*-wave velocity (m s^{-1}); ρ = density (kg m^{-3}); σ = Poisson's ratio.
**Medium grained sand layer as indicate in Khadka (1993). See Geology paragraph (Section 2) and Discussion (Section 6).

general trend, where the southern maximum is elongated in a NW–SE direction, compatible with the geological structure of the area (Sakai *et al.* 2006, 2015). The separation belt between the two maxima coincides with the location of the Chobar fault (Trevisani *et al.* 2021) conditioning the sedimentary sequence and the basement morphology (Asahi 2003).

Rough estimations of the average *Vs* of the whole basin stratigraphic sequence, were made by the HVSR measurements near the borehole BH1 (Table 2, Fig. S2a), with 252 m depth (Sakai *et al.* (2001) and a frequency resonance peak $f = 0.6$ Hz (Table 1), and the borehole at Ratna Park near the BR (Table 2, Fig. S2b), reaching 550 m depth (Khadka 1993) and a frequency of $f = 0.275$ Hz. While the velocities computed by the simple formula $Vs = 4Hf$ are surprisingly the same ($Vs = 605$ m s^{-1}), in the other cases by inversions there are small differences. For each site, the former inversion is with tight constraints, while the second with fixed basin thickness. For BH1, in the first case the result of the Parolai *et al.* (2005) inversion gives an average *Vs* value of 610 ± 39 m s^{-1} and a thickness of 255 m (Table 2, Fig. S2a), instead Ratna Park provides an average *Vs* value of 647 ± 28 m s^{-1} and a thickness of 543 m (Table 2, Fig. S2b). With fixed thickness the differences are irrelevant. All the *Vs* for the weathered bedrock are over 850 m s^{-1}. These *Vs* results, obtained from HVSR surveys close to the boreholes, will be used as constrains in subsequent inversions.

The azimuthal independence of Ratna Park (Fig. 6a), Apeiron House (6b) and Baluwatal (6c), shows the 1-D response of the deepest part of the basin, as the 1-D inversions well explain. It is not the same for the BH1 site, where the azimuthal rotation analysis shows a slight 2-D effect (Fig. 6d) more evident for BH2 (6e), probably due to the proximity to the western edge of the basin with a more complex stratigraphic situation and less thickness (Dill *et al.* 2001). This probably explains the differences in the mean *Vs* values between Ratna Park and BH1.

We analysed the azimuthal spectra of other sites (as NSET, S04) from the deepest part of the basin, confirming azimuthal independence, while other sites in the Lalitpur area (as S06, S16) show azimuthal behaviour similar to BH1 and BH2. The map of Fig. 10, confirms these assumptions, showing a distribution of azimuthal independent sites (white dots) inside the deeper part of the basin. The contour line borders the RP of 2 s so its interior corresponds to depths more than 300 m. The red dots indicate sites with azimuthal dependence, while the orange dots indicate ambiguity. From this analysis, it can be assumed that the seismic response of the deep part of the basin, with high values of period T, depends only on the stratigraphy of the fluvio-lacustrine sediments and would explain the long period pulses recorded from the strong motion data of the Gorkha earthquake. In contrast, at the edges, the response is influenced by the complex structure of the basin.

The values of *Vs* in the basement, reported in Table 2 may appear underestimated; however, we preferred not to use tight constraints, and although the basement rocks are comprised of metamorphic rocks (Green Phyllite, see Khadka 1993), usually with higher velocities (>2000 m s^{-1}), we obtained a value around 900 m s^{-1} (Table 2). We assumed that the upper part of the basement is altered and fractured, thus lowering its mechanical properties and the associated *Vs* velocity. Takai *et al.* (2016) noted for the rocks below KTP station: 'The tested velocity of *S* waves at a depth of 10 m was over 700 m s^{-1} at the KTP site, but it was less than 200 m s^{-1} at the other three sites'. This occurrence is also confirmed by Bijukchhen *et al.* (2017). A $f = 0.35$ Hz frequency peak with an amplitude 3.8

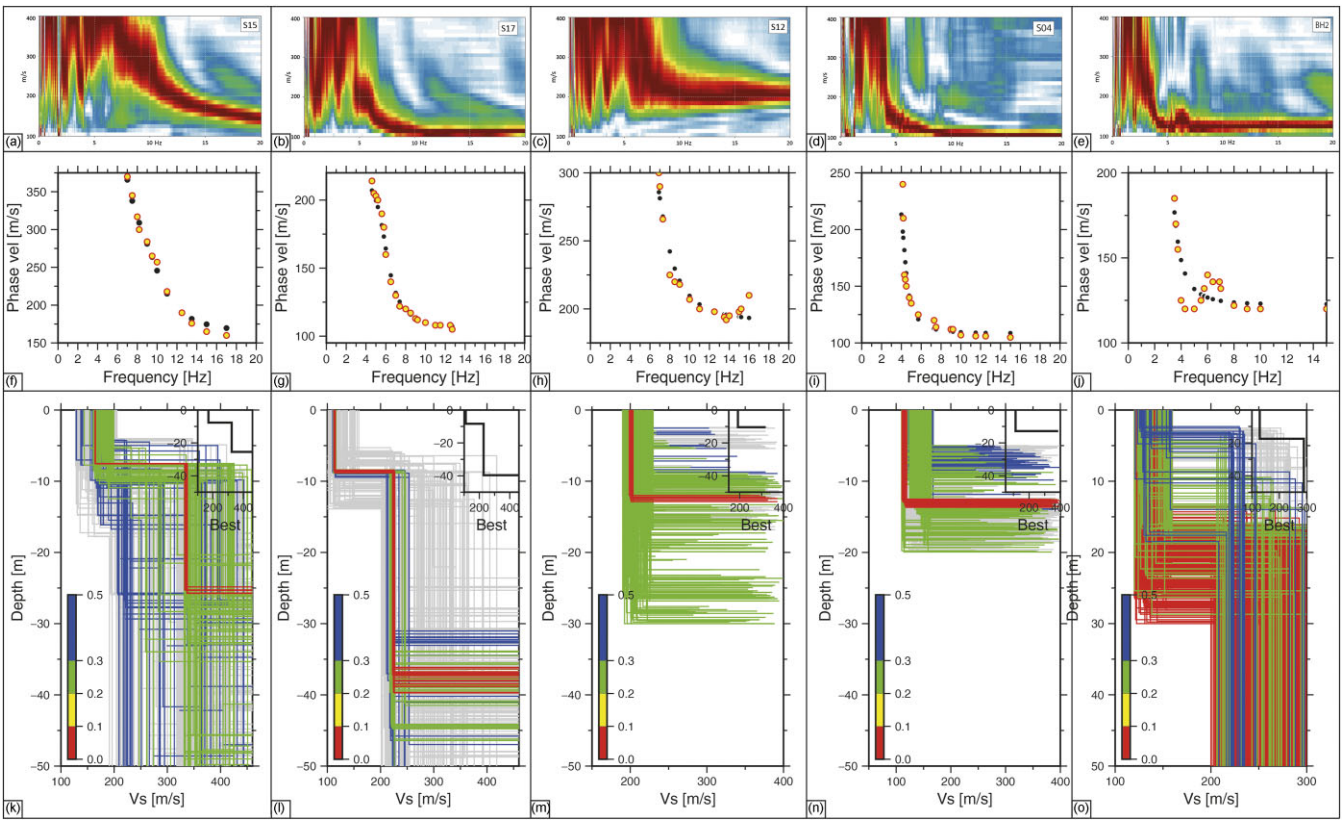

Figure 8. *Vs* profiles of sites S15, S17, S12, S04 and BH2 (a–e) from the ReMi^{TM} surveys carried out during the 2015 NSET-OGS campaign (Sandron *et al.* 2019), recorded by Rosina equipment and elaborated by Grilla software; ReMi^{TM} velocities (f–j) evaluated by inversion (Parolai *et al.* 2005); coloured dots: experimental data; grey dots forward model of inversions. *Vs*—depth profiles (k–o) (colours indicate models lying within a certain percentage of the minimum misfit); in the small box: black profile represents the minimum misfit model. For the sake of comparison with other profiles, Fig. 10(k) represents only the first 30 m of the BH2 profile, the inversion of which is in agreement with that of Sandron *et al.* (2019, fig. 8).

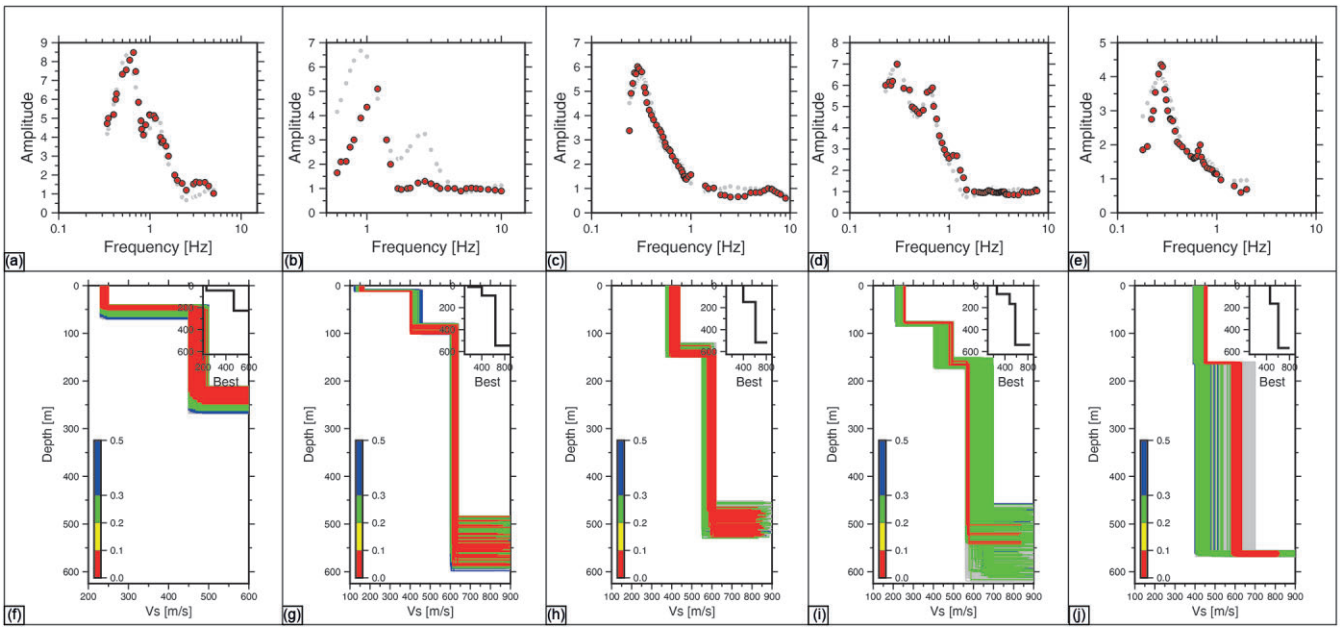

Figure 9. HVSR inversion curves showing two peaks using Parolai *et al.* (2005) approach: (a–e): experimental curve (red dots) and forward model (grey dost); (f–j) resulting *Vs* depth profiles by Parolai *et al.* (2005) inversion method; (colours indicate models lying within a certain percentage of the minimum misfit). In the small box: black profile represents the minimum misfit model. The corresponding sites are: S16 [16] Figs (a, f); S02 [02] (b, g); NSET HQ [21] (c, h); BH2 [22] (d, i) and Ratna Park [30] (e, j). The numbers in square brackets are the site number of Table 1 and Fig. 4.

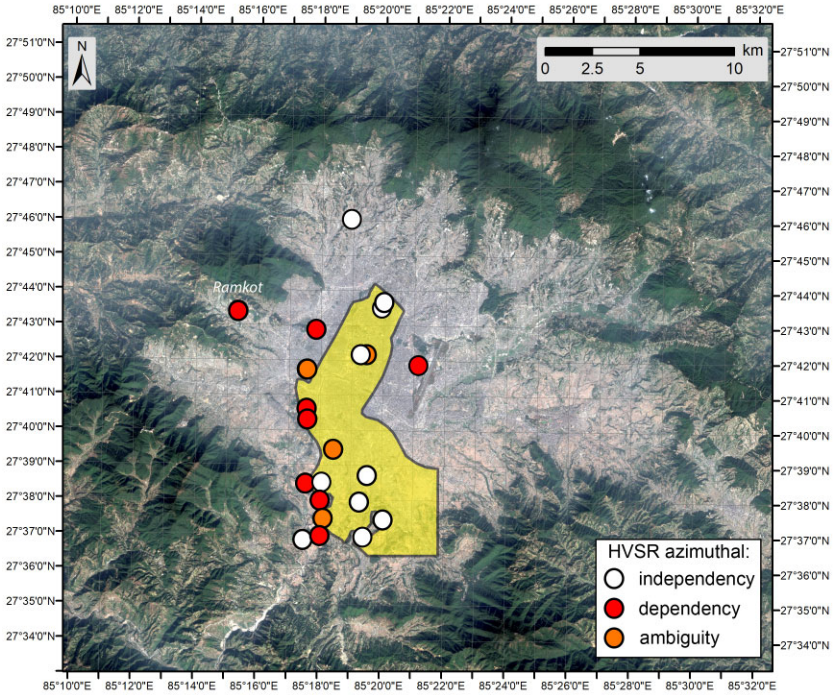

Figure 10. Map of the sites where the HVSR azimuthal spectra are calculated. White dots the sites with not azimuthal dependency (1-D behaviour); red dots the sites with azimuthal dependency; orange dots ambiguity. The yellow area is the deeper part of the basin. The contour curve corresponds to the resonance period RP = 2 s, which corresponds to depths more than 300 m (see Fig. 4). The map shows the 1-D response of the basin in its deeper part depends only on the impedance contrast between an altered basement and the overlying fluvio-lacustrine sediment stack. In contrast, at the edges, the response is influenced by the complex structure of the basin.

and minor deviation, are shown for BH1 site in Fig. 5(c). This peak could be associated with the top of a compact basement.

We also analysed the dispersion curves of the seismic arrays (Tables 3, 4, S1 and Figs 7 and 8). In Sandron *et al.* (2019), we have shown only the V_{RP} dispersion curves from ReMi^{TM} and a qualitative assessment of phase velocities. Here, by two independent methods, namely Dinver (Wathelet 2005) and Parolai *et al.* (2005), we obtain the evaluations for the near-surface *Vs*. In Fig. 7 there are the results of the arrays of NSET HQ and Ratna Park, with the resulting comparison between the two methods applied to the same velocity models. For the simplified model of the well stratigraphy of NSET HQ, the outcomes (Table 3) are comparable to those of a simplified model for Ratna Park from Khadka (1993) (Table 4). Figs 8 and S3 show the joint inversions by Parolai *et al.* (2005) methods of some dispersion curves of the 2015 survey. All the results always show a first layer with a low *Vs* around 120–160 m s^{-1} lying on a deeper layer with *Vs* of around 200–400 m s^{-1}. The thicknesses of the layers are variable depending on the area. The presence of these uppermost layers is also confirmed by Molnar *et al.* (2017) and from the stratigraphy of the first 30 m of the well near the NSET HQ. Poovarodom *et al.* (2017) found similar *Vs* values on five sites in the central-northern part of the basin, by inversions of five arrays, for the first 30 m.

The long-time HVSR surveys with sensors such as the Trillium 20 s are more compatible with the dimensions of a great and complex basin such as Kathmandu valley. Gilder *et al.* (2020) reported: 'the microtremor data (Paudyal *et al.* 2013), when compared to the borehole records, appear to represent the boundary between the Kalimati Formation (the homogeneous silt deposit) and any other underlying sequence'. Paudyal *et al.* (2013) probably detected this reflector using their sensors. This situation is typical of deep sedimentary basins, such as the central Po Plain in Northern Italy (Paolucci *et al.* 2015), where the authors explain these higher frequency peaks HVSR peaks assuming the presence of impedance contrasts within the Quaternary coverage, probably caused by major climate changes. The purpose of HVSR inversions in Figs 9 and Table S2 is to confirm the hypothesis of the possible strong impedance contrast already discussed in Sandron *et al.* (2019) and reported in this paper in Section 2.1. This hypothesis, that the climatic changes during Late Pleistocene (Mukunda & Sakai 2008; Mampuku *et al.* 2008), modified the geotechnical conditions of the layers. The HVSR comparison of Figs 9(a)–(e) shows good overlapping, especially for BH2 and also for S16 and NSET-EQ. Profiles of *Vs* versus depth (Figs 9f–j) show a rapid increase in *Vs* from 200–460 m s^{-1} to about 600 m s^{-1} in the NSET and Ratna Park (where the basement is very deep) areas at depths of 148 and 164 m, respectively. The *Vs* below this supposed interface (611–605 m s^{-1}) are consistent with those computed by HVSR close to the two boreholes BH1 and in Ratna Park. Site S16 is doubtful as the main peak occurs at $f = 0.629$ Hz and *Vs* in the deepest layers is 686 m s^{-1}. But as for site S02, which shows an important peak at $f = 1.2$ Hz, the inversions are directed mainly to the first part of the stratigraphic sequence, which agree with the results of Tables 3, 4, S1 and Fig. 8. Fig. S4 is an interpretation of all performed inversions, showing a consistent stratigraphic correlation with a coherent variation in depth of the high seismic impedance layer of Quaternary age. The only trend that differs is for the S16 site, but the area of Lalitpur has a discontinuous trend. The short segments denoted 'P' are the hypothetic depths calculated with Paudyal *et al.* (2013) frequencies and the corresponding *Vs* of Table S2. There is a coincidence only

for BH2 and for Ratna Park (not shows if the Fig. S4), with a peak at $f = 0.68$ Hz and *Vs* of Table S2, the depth is 164–166 m.

7 CONCLUSIONS

This work can be considered a comprehensive summary of the two measurement campaigns conducted by NSET–OGS after the Gorkha earthquake. Some indications arising during the first analysis of data were confirmed by the second integrative set of specific measurements. We demonstrated:

(i) The HVSR data set analysed in this work mainly outlines the distribution of the resonance periods in the Kathmandu basin with values greater than $T = 2$ s, with two local maxima with $T > 3$ s, but also areas with great variability;

(ii) The additional measurements confirmed the pattern of the basement topography that we attempted to infer with a geostatistics extrapolation in our previous work (Trevisani *et al.* 2021);

(iii) The HVSR response of the deepest part of the basin is 1-D, with a rough estimation of the average *Vs*, approximately 600–650 m s^{-1}, (near Ratna Park), representing values for all the fluvio-lacustrine stratigraphic sequence. Below these clayey sediments the first weathered rocks of the basement shows *Vs* around 900 m s^{-1};

(iv) The azimuthal independence of the Ratna Park HVSR inversion, located in the deepest part of the basin, confirms the validity of inversions at the previous point 3 and the *Vs* assessment of the entire basin sediment sequence. It suggests that the seismic response in the deep part of the basin is due to an impedance contrast between an altered basement and the overlying sediment stack. Concerning the Gorkha 2015 strong ground motion records, our results corroborate the idea of the presence of a pulse in the 3–6 s range in the basin data, clearly established as a combination of the earthquake's source and the basin response effect itself. As already highlighted by Takai *et al.* (2016) and Rupakhety *et al.* (2017), we agree that the basin structure is complex, and a definitive conclusion is premature. However, for its deepest part an approximately 1-D structure is in agreement with Dhakal *et al.* (2016), while at the outskirts and in the Lalitpur area, morphological sedimentary factors take over;

(v) The *Vs* in the shallower deposits, analysing the dispersion curves of the seismic arrays by two independent methods, is less than 160 m s^{-1} in the topmost layer, being slightly higher than 200 m s^{-1} in the underlying layer, as confirmed by other studies (Molnar *et al.* 2017; Poovarodom *et al.* 2017).

(vi) The multiple high frequency peaks visible in the HVSR curves at some sites suggest the possible presence of a sharp increase in *Vs* at intermediate depths, with sufficient seismic impedance to produce peaks at frequencies $f > 0.5$ Hz and above 1 Hz. This layer could explain the high frequency peaks reported in Paudyal *et al.* (2012, 2013), already discussed in Sandron *et al.* (2019).

DATA AND RESOURCES

The seismic noise data (H/V and arrays) used in this paper are available upon request from the authors.

ACKNOWLEDGMENTS

This work was partly supported by the Region FVG (Friuli Venezia Giulia - Italy), Regional Law 19/2000, International Development Cooperation and Partnership Activities 2014–2017, Decree no. 1134/SG 11.27.2017, IN-EPAL MICRO Project; https://www.regione.fvg.it/rafvg/cms/RAFVG/fondi-europei-fvg-internazionale/cooperazione-internazionale-sviluppo/FOGLIA69/. The two institutions involved with this study also supported the surveys. Many thanks are due to Livio Sirovich for discussions concerning the lacustrine sediments and the hypothesis of the interface of contrast of impedance at the middle deep. Sebastiano Trevisani, Roberto Francese and Stefano Picotti are thanked for their valuable suggestions, Alberto Tamaro for a GIS support. Stefano Parolai for the suggestions and the availability of its codes for representing the uncertainties of the inversion results. We remember Marco Mucciarelli as inspiring the first of our missions to Kathmandu.

FP, DKM, SP, DS, MG and SNS organized the surveys; FP, SP, DS, SW, CC and MG performed the surveys; FP, DKM, DS carried out the computations and interpretation of data; FP, DS and MG wrote the paper.

REFERENCES

Adhikari, L.B. *et al.*, 2015. The aftershock sequence of the 2015 April 25 Gorkha-Nepal earthquake, *Geophys. J. Int.,* **203,** 2119–2124.

Aki, K., 1957. Space and time spectra of stationary stochastic waves, with special references to microtremors, *Bull. Earthq. Res. Inst.,* **35,** 415–457.

Arai, H. & Tokimatsu, K., 2004. S-wave velocity profiling by inversion of microtremor H/V spectrum, *Bull. seism. Soc. Am.,* **94,** 53–63.

Arai, H. & Tokimatsu, K., 2005. S-wave velocity profiling by joint inversion of microtremor dispersion curve and horizontal-to-vertical (H/V) spectrum, *Bull. seism. Soc. Am.,* **95,** 1766–1778.

Asahi, K. 2003. Thankot active fault in the Kathmandu valley, Nepal Himalaya, *J Nepal Geol. Soc*., **28,** 1–8.

Avouac, J.P., Meng, L., Wei, S., Wangand, T. & Ampuero, J.P., 2015. Lower edge of locked Main Himalayan Thrust unzipped by the 2015 Gorkha earthquake, *Nat. Geosci. Lett.,* **8,** 708–711.

Bäth, M., 1973. *Introduction to Seismology,* A. Haldsted Press Book, pp. 395.

Bettig, B.P., Bard, Y., Scherbaum, F., Riepl, J., Cotton, F., Cornou, C. & Hatzfeld, D., 2001. Analysis of dense array measurements using the modified spatial auto-correlation method (SPAC). Application to Grenoble area, *Boll. Geof. Teor. Appl.,* **42**(3-4), 281–304.

Bhattarai, M., Adhikari, L.B., Gautam, U.P., Laurendeau, A., Labonne, C., Hoste-Colomer, R., Sèbe, O. & Hernandez, B., 2015. Overview of the Large 25 April 2015 Gorkha, Nepal, earthquake from accelerometric perspectives, *Seismol. Res. Lett.,* **86**(6), 1540–1547.

Bijukchhen, S.M., Takai, N. & Shigefuji, M., 2017. Estimation of 1-D velocity models beneath strong-motion observation sites in the Kathmandu Valley using strong-motion records from moderate-sized earthquakes, *Earth, Planets Space,* **69**(97), 1–16.

Bollinger, L. *et al.*, 2014. Estimating the return times of great Himalayan earthquakes in eastern Nepal: evident from the Patu and Bardibas strands of the Main Frontal Thrust, *J. geophys. Res.,* **119,** 7123–7163.

Bollinger, L., Tapponnier, P., Sapkota, S.N. & Klinger, Y., 2016. Split deficit in central Nepal: omen for a repeat of the 1344 AD earthquake?, *Earth Planets Space,* **68,** doi:10.1186/s40623-016-0389-1.

Bonnefoy-Claudet, S., Cotton, F. & Bard, P.Y., 2006a. The nature of seismic noise wavefield and its implications for site effects studies. A literature review, *Earth-Sci. Rev.,* **79**(3), 205–227.

Bonnefoy-Claudet, S., Cornou, C., Bard, P.Y., Cotton, F., Moczo, P., Kristek, J. & Fah, D., 2006b. H/V ratio: a tool for site effects evaluation. Results form 1-D noise simulation, *Geophys. J. Int.,* **167,** 827–837.

Boxberger, T., Picozzi, M. & Parolai, S., 2011. Shallow geology characterization using Rayleigh and love wave dispersion curves derived by seismic noise array measurements, *J. appl. Geophys.,* **75**(2), 345–354.

Capon, J., 1969. High-resolution frequency-wavenumber spectrum analysis, *Geophysics,* **34**(1), 21–38.

Dhakal, Y.P., Kubo, H., Suzuki, W., Kunugi, T., Aoi, S. & Fujiwara, H., 2016. Analysis of strong ground motions and site effects at Kantipath, Kathmandu, from 2015 Mw 7.8 Gorkha, Nepal, earthquake and its aftershocks, *Earth, Planet Space,* **68,** 68–58.

Dill, H.G., Kharel, B.D., Singh, V.K., Piya, B. & Geyh, M., 2001. Sedimentology and paleogeographic evolution of the intermontane Kathmandu basin, Nepal, during the Pliocene and Quaternary. Implications for formation of deposits of economic interest, 2001, *J. Asian Earth Sci.,* **19**(2001), 777–804.

Dixit, A. *et al.*, 2015. Strong-Motion Observations of the M 7.8 Gorkha, Nepal, earthquake sequence and development of the N-SHAKE strong-motion network, *Seismol. Res. Lett.,* **86**(6), 1533–1539.

Ewing, W.M., Jardetzky, W.S. & Press, F., 1957. *Elastic Waves in Layered Media,* McGraw-Hill, Inc., pp. 380.

Feng, G., Li, Z., Shan, X., Zhang, L., Zhang, G. & Zhu, J., 2015. Geodetic model of the 2015 April 25 M_w 7.8 Gorkha Nepal earthquake and M_w 7.3 aftershock estimated from InSAR and GPS data, *Geophys. J. Int.,* **203,** 896–900.

Foti, S. *et al.*, 2018. Guidelines for the good practice of surface wave analysis: a product of the InterPACIFIC project, *Bull. Earthq. Eng.,* **16,** 2367–2420.

Galetzka, J. *et al.*, 2015. Slip pulse and resonance of the Kathmandu basin during the 2015 Gorkha earthquake, Nepal, *Science,* **349**(6252), 1091–1095.

Gilder, C.E.L. *et al.*, 2020. The SAFER geodatabase for the Kathmandu Valley: geotechnical and geological variability, *Earth Spectra,* **36**(3), 1549–1569.

GIPP group GFZ Potsdam. https://www.gfz-potsdam.de/en/section/geophysical-deep-sounding/infrastructure/geophysical-instrument-pool-potsdam-gipp/.

Hobiger, M. *et al.*, 2013. Ground structure imaging by inversions of Rayleigh wave ellipticity: sensitivity analysis and application to European strong-motion sites, *Geophys. J. Int.,* **192**(1), 207–229.

Khadka, M.S., 1993. The groundwater quality situation in alluvial aquifers of the Kathmandu Valley, Nepal. AGSO, *J. Aust. Geol. Geophys.,* **14**(2/3), 207–211.

Konno, K. & Omachi, T., 1998. Ground-motion characteristics estimated from spectral ratio between horizontal and vertical components of microtremors, *Bull. seism. Soc. Am.,* **88,** 1, 228–241.

Igarashi, Y., Yoshida, M. & Tabata, H., 1988. History of vegetation and climate in the Kathmandu valley, *Proc. Indian Nat. Sci. Acad.,* **54**(4), 550–563.

Louie, J., 2001. Faster, better: shear-wave velocity to 100 meters depth from refraction microtremor arrays, *Bull. seism. Soc. Am.,* **91,** 347–364.

Mampuku, M., Yamanaka, T., Uchida, M., Fujii, R. & Maki, T., 2008. Changes in C3/C4 vegetation in the continental interior of the Central Himalayas associated with monsoonal paleoclimatic changes during the last 600 kyr, *Clim. Past.,* **4,** 1–9.

Molnar, P. & Tapponnier, P., 1975. Cenozoic tectonics of Asia: effects of a continental collision, *Science,* **189**(4201), 419–426.

Molnar, S., Onwuemeka, J. & Adhikari, S.R., 2017. Rapid post-earthquake microtremor measurements for siter amplification and shear wave velocity profiling in Kathmandu, Nepal, *Earthq. Spectra,* **33**(1), S55–S72.

Moribayashi, S. & Maruo, Y., 1980. Basement topography of the Kathmandu Valley, Nepal – an application of the gravitational method to the survey of a tectonic basin in the Himalaya, *J. Japan Soc. Eng. Geol.,* **21,** 30–37.

Mukunda, R.P. & Sakai, H., 2008. Stratigraphy and depositional environments of basin-fill sediments in southern Kathmandu Valley, Central Nepal, *Bull. Depart. Geol.,* **11,** 61–70.

Nakamura, Y., 1989. A method for dynamic characteristic estimation of subsurface using microtremors on the ground surface, *Quart. Rep. Railway Tech. Res. Inst.,* **30,** 25–33.

Nakamura, Y., 2000. Clear identification of fundamental idea of Nakamura's technique and its applications, in *Proceedings of the 12thWorld Conference on Earthquake Engineering,* Auckland, New Zeeland.

Nakamura, Y., 2019. What is the Nakamura method?, *Seismol. Res. Lett.,* **90,** 1437–1443.

Nogoshi, M. & Igarashi, T., 1971. On the amplitude characteristics of microtremor (Part 2), *J. Seism. Soc. Japan,* **24,** 26–40.

Noguchi, S. & Sasatani, T., 2008 Quantification of degree of nonlinear site response, in *Proceedings of the 14th World Conference on Earthquake Engineering,* Beijing, Paper no. 03-03-0049, pp. 2323–2332.

Pandey, M.R., 2000. Ground response of Kathmandu valley on the basis of microtremors, in *Proceedings of the 12th World Conference on Earthquake Engineering,* Auckland, New Zealand, 30 Jan–4 Feb 2000, Paper no. 2106.

Paolucci, E., Albarello, D., D'Amico, S., Lunedei, E., Martelli, L., Mucciarelli, M. & Pileggi, D., 2015. A large scale ambient vibration survey in the area damaged by May-June 2012 seismic sequence in Emilia Romagna, Italy, *Bull. Earthq. Eng.,* **13**(11), 3187–3206.

Park, C.B., Miller, R.D. & Xia, J., 1997, Multi-channel analysis of surface waves (MASW), "A summary report of technical aspects, experimental results, and perspective", Open-file Report #97-10, Kansas Geological Survey.

Parolai, S., Bormann, P. & Milkerei, C., 2001. Assessment of the natural frequency of the sedimentary cover in the Cologne area (Germany) using noise measurements, *J. Earthq. Eng.,* **5,** 541–564.

Parolai, S., Picozzi, M., Richwalski, S.M. & Milkereit, C., 2005. Joint inversion of phase velocity dispersion and H/V ratio curves from seismic noise recordings using a genetic algorithm, considering higher modes, *Geophys. Res. Lett.,* **32**(1), doi:10.1029/2004GL021115.

Parolai, S., Maesano, F. E., Basili, R., Silacheva, N., Boxberger, T. & Pilz, M., 2019. Fingerprint identification using noise in the horizonthal-to-vertical spectra ratio: retrieving the impedance contrast structure for the Almaty Basin (Kazakhstan), *Front. Earth Sci.,* **7,** doi:10.3389/feart.2019.00336.

Paudyal, Y.R., Bhandary, N.P. & Yatabe, R., 2012. Seismic microzonation of densely populated area of Kathmandu Valley of Nepal using microtremors observations, *Earthq. Eng.,* **16**(8), 1208–1229.

Paudyal, Y.R., Yatabe, R., Bhandary, N.P. & Dahal, R.K., 2013. Basement topography of the Kathmandu Basin using microtremor observation, *J. Asian Earth. Sci.,* **62,** 627–637.

Pettenati, F., Sirovich, L. & Bjerrum, L. W., 2017. Fault sources and kinematics of the 1897 Assam (M_W8.1) and the 1934 Nepal (M_S8.2) earthquakes retrieved by *KF*-NGA inversion and their seismotectonic implications, **107**(5), 2480–2489.

Poovarodom, N., Chamlagain, D., Jirasakjamroonsri, A. & Warnitchai, P., 2017. Site characteristics of Kathmandu Valley from array microtremor observations, *Earthq. Spectra,* **33**(21), S85–S93.

Rupakhety, R., Olafsson, S. & Halldorsson, B., 2017. The 2015 Mw 7.8 Gorkha Earthquake in Nepal and its aftershocks: analysis of strong ground motion, *Bull. Earthq. Eng.,* **15,** 2587–2616.

Sakai, H., Fujii, R., Kuwahara, Y., Upreti, B.N. & Shrestha, S.D., 2001. Core drilling of the basin-fill sediments in the Kathmandu Valley for palaeoclimatic study: preliminary results, Nepal, *J. Nepal Geol. Soc.,* **25,** 9–18.

Sakai, H., Yahagi, W., Fujii, R., Hayashi, T. & Upreti, B.N., 2006. Pleistocene rapid uplift of the Himalayan frontal ranges recorded in the Kathmandu and Siwalik basins, *Palaeogeog. Palaeoclimat. Palaeoecol.,* **241**(1), 16–27.

Sakai, H., Gajurel, A.P., Upreti, B.N., Tabata, H., Ooi, N. & Kitagawa, H., 2008. Revised lithostratigraphy of fluvio-lacustrine sediments comprising northern Kathmandu basin in central Nepal, *J. Nepal Geolog. Soc.,* **37,** 2008–44.

Sakai, T., Gajurel, A.P. & Tabata, H., 2015. Seismites in the Pleistocene succession and recurrence period of large earthquakes in the Kathmandu Valley, Nepal, *Geoenviron. Disasters,* **2,** 25.

Sandron, D., Maskey, S., Giorgi, M., Maharjan, D.K., Shrestha, S.N., Cravos, C. & Pettenati, F., 2019. Environmental noise measures in Lalitpur area (Kathmandu) after 1 M7.8 Gorkha 2015 earthquake, *Boll. Geof. Teorica Appl.,* **60**(1), 17–38.

Sambridge, M., 1999. Geophysical inversion with a neighbourhood algorithm: I. Searching a parameter space, *Geophys. J. Int.,* **138,** 479–494.

Sapkota, N.S., Bollinger, L., Klinger, Y., Tapponnier, P., Gaudemer, Y. & Tiwar, D., 2013: Primary surface ruptures of the great Himalayan earthquakes in 1934 and 1255, *Nat. Geosci.,* **6,** 71–76.

SESAME, 2004. Guidelines for the implementation of the H/V spectral ratio technique on ambient vibrations: measurements, processing and interpretation, 2004, SESAME European Research Project WP12, deliverable no. D23.12 ftp://ftp.geo.uib.no/pub/seismo/SOFTWARE/SESAME/USER-GUIDELINES/SESAME-HV-Userlines.pdf, last access March 13, 2018.

Shrestha, S. & Shah, R.S., 2014. Shallow Aquifer Mapping of Kathmandu Valley, 2014, A Final Report, submitted to Groundwater Resources Development Board, Babarmahal, Kathmandu, 51pp.

Sibson, R., 1981. A brief description of natural neighbor interpolation, in *Interpreting Multivariate Data,* pp. 21–36, ed. Barnett, V., John Wiley & Sons.

Takai, N., Shigefuji, M., Rajaure, S., Bijukchhen, S., Ichiyanagi, M., Dhital, M.R. & Sasatani, T., 2016. Strong ground motion in the Kathmandu Valley during the 2015 Gorkha, Nepal, Earthquake, *Earth Planets Space,* **68,** doi:10.1186/s40623-016-0383-7.

Tuan, T.T., Scherbaum, F. & Malischewsky, P.G., 2011. On the relationship of peaks and troughs of the ellipticity (*H/V*) of Rayleigh waves and the transmission response of single layer over half-space models, *Geophys. J. Int.,* **184,** 793–800.

Trevisani, S., Maharian, D.K., Sandron, D., Shrestha, S.N., Paudyal, S., Pettenati, F. & Giorgi, M., 2020. Geostructural complexity and passive seismic surveys: a geostatistical analysis in the *Kathmandu basin*, in *Proceedings of the 22nd EGU General Assembly,* held online 4-8 May, 2020, EGU2020-7117.

Trevisani, S., Pettenati, F., Paudyal, S. & Sandron, D., 2021. Mapping long period soil resonances in the Kathmandu basin using microtremors, *Environ. Earth Sci.,* **80**.

Wathelet, M., 2005. Array recordings of ambient vibrations: surface-wave inversion, *PhD thesis*, University de Liege, Belgium.

Wesnousky, S., Kumahara, G.Y., Chamlagain, D., Pierce, I.K., Karki, A. & Gautam, D., 2017. Geological observations on large earthquakes along the Himalayan frontal fault near Kathmandu Nepal, *Earth planet. Sci. Lett.,* **457,** 366–375.

SUPPORTING INFORMATION

Supplementary data are available at *GJI* online.

Figure S1. (a) Histogram of the 42 HVSR resonance peak periods RPs, sorted also by instrument type; (b) Configuration of the array deployed in Ratna Park, map by the Dinver of Geopsy package (Wathelet 2005) The numbers are the code of Cube-3ch-recorders. These recorders were connected with: c0AAS—Lennartz 1 s; c0844 and c0845 3–channels PE-6/B-3C-4.5 Hz; c0166, c0167, c0168–vertical 4.5 Hz geophones.

Figure S2. HVSR data inversions at: (a) BH1 well; (b) Ratna Park, close to the BR well. The red curve is the Forward model of inversion; black is the experimental curve with the standard deviation. Experimental HVSR are in black, the forward models of inversion results are in red. The two wells reaching the basement and the HVSR inversions were used to estimate the average *S*-wave velocity representative of all fluvio-lacustrine stratigraphic sequence.use tight constraints only for first layer

Figure S3: HVSR of joint inversion of Figs 8, for S15(a) and S17 (b) which are the only models with high frequency peaks over 2 values of amplitude. Red dots: experimental data; grey dots: forward models.

Figure S4. Seismic-stratigraphic correlogram among the sites used for the HVSR inversions of second peaks (Fig. 9). The 8 sites are in a line from south to north in the western part of the basin (follows the circled numbers in Fig. 4). The dashed line marks the hypothetic high seismic impedance layer of Quaternary age which generates the secondary HVSR peaks Figs 9(a)–(j). The dashed columns are the stratigraphic sequences below the hypothetic reflectors, while the dotted columns of S16 and S06 are outside the inversions assessments. The reference depth of the basement is the column of BH1 (252 m). The short 'P' segments stand for the hypothetic depths calculated with Paudyal *et al.* (2013) frequency by the correspondent *Vs* of raw 5, Table S2).

Table S1. Inversion results of the Rayleigh dispersion curves, from ReMi^{TM} method and related interpretation at various sites. The depths are reported in the brackets ().

Table S2. Inversion results of the HVSR spectra showing multipeaks and related interpretation at various sites. The depths are reported in the brackets ().